# 1

# Graphene for Silicon Optoelectronics

## 1.1 Introduction

Rich electronic, optical, and mechanical properties of graphene, such as high carrier mobilities, optical transparency, flexibility, robustness, and environmental stability, offer solutions to many technological challenges in the communication, health, and energy sectors. Unique characteristics of Dirac fermions in graphene enable specific integer and fractional hall effects, minimum conductivity of $\sim 4e^2/\hbar$, and near ballistic transport at room temperature [1]. In specific, the true potential of graphene lies in optoelectronics and photonics [2], where intrinsic properties such as linear dispersion of Dirac electrons enabling ultrawideband tunability, transmittance expressed in terms of fine-structure constant, saturable absorption due to Pauli blocking, and hot luminescence originating from nonequilibrium carriers enable highly efficient physical mechanisms at the interest of condensed matter physics and the optoelectronic applications.

The present image sensor market is dominated by the Si detectors integrated with CMOS readout circuits, offering high resolution, compact footprint, low manufacturing cost, and high performance [3]. As silicon, in general, is the active material in these systems, the absorption bandwidth is limited to visible to infrared light (300–900 nm). Some crucial applications of image sensors, such as biomedical imaging, gas sensing, spectroscopy, environmental monitoring, and night vision, require a broad operating range in the infrared region that can even extend to the terahertz region [4].

In addition, many of these applications need the detector's operation in both visible and infrared, where emerging applications such as 3D imaging for autonomous vehicles and augmented virtual reality systems benefit. Specifically, the extension of 3D imaging into the infrared range reduces interference with the strong visible background light and thus helps reduce the overall power consumption [2]. These applications need novel photodetectors with a broad wavelength range, high detectivity, low power, low production cost, and easy integration with Si CMOS technology. Graphene and the related two-dimensional (2D) material-based photodetectors fulfill all these requirements and offer a fast-broadband response from ultraviolet to

*Graphene for Post-Moore Silicon Optoelectronics,* First Edition. Yang Xu, Khurram Shehzad, Srikrishna Chanakya Bodepudi, Ali Imran, and Bin Yu.
© 2023 WILEY-VCH GmbH. Published 2023 by WILEY-VCH GmbH.

COPYRIGHTED MATERIAL

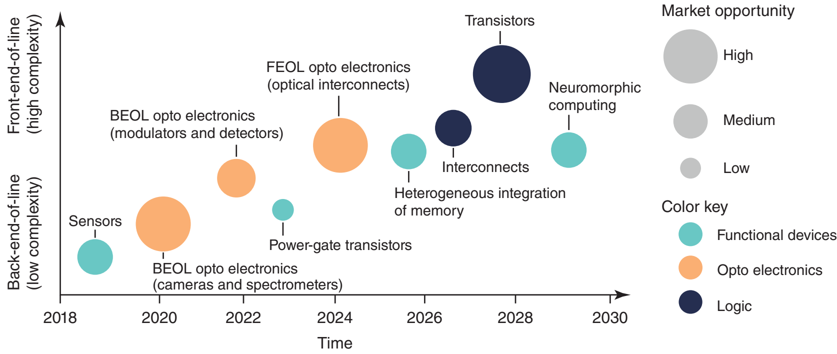


**Figure 1.1** Application of two-dimensional materials-silicon technology depicted in time and the complexity for integration. Source: Reproduced with permission from Akinwande et al. [2]; Springer Nature.

terahertz spectral range (Figure 1.1). The emerging applications in optoelectronics and future neuromorphic and quantum computing devices seek 2D materials integrated with the Si CMOS process to address the most pressing challenges and limitations faced by miniaturization in Si technology.

Low power consumption, high operating speeds, and efficient energy transduction are the primary requirements for the next-generation electronic and optoelectronic devices, where graphene made its mark as a future material with the potential to resolve the limitations of silicon electronics. Developing device schemes by integrating graphene and silicon allows us to continue to use the most successful Si technology while exploiting the benefits of graphene to improve the existing device's performance and efficiency; graphene electronics is strongly connected with silicon and CMOS technology. For instance, the ability to visualize atomic layer thick graphene on $SiO_2$/Si substrate is the most crucial step in investigating the transport properties of graphene. Let us start our discussion with this fundamental step of identifying graphene and absorbing light.

## 1.2 Optical Absorption

The contrast in the optical image can be used to identify graphene in the Si/$SiO_2$ substrate, which results from interference with $SiO_2$ as a spacer layer and scales with the number of graphene layers. This contrast can be further tuned by varying the spacer thickness or wavelength of light. Graphene with fixed universal optical conductance $G_0 = e^2/(4\hbar) = 6.08\times10^{-5}$ gives the transmittance,

$$T = \left(1 + 0.5\pi\alpha\right)^{-2} \partial \approx 1 - \pi\alpha \approx 97.7\% \tag{1.1}$$

where $\alpha = e^2/(4\pi\varepsilon_0\hbar c) = G_0/\pi\varepsilon_0 c = 1/137$ is the fine-structure constant. The optical absorbance is proportional to the layer number, with each layer absorbing 2.3% of the visible spectrum. Graphene exhibits an almost flat absorption spectrum from

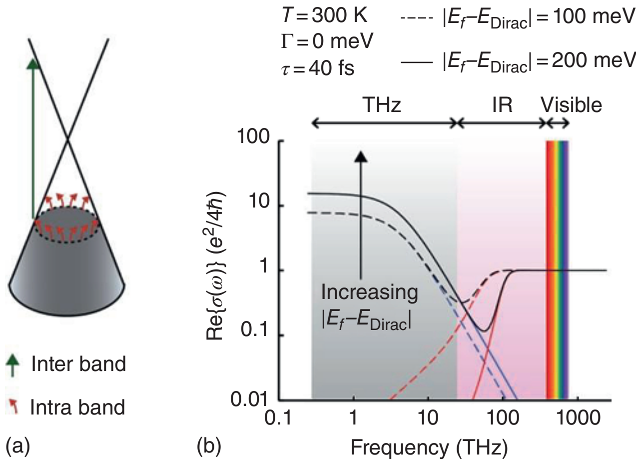


**Figure 1.2** (a) Optical transitions in graphene. (b) Optical conductivity versus frequency of graphene from terahertz to visible region. Source: Reproduced with permission from Sensale-Rodriguez [5]; IEEE.

300 nm to 2.5 μm, with a peak in the ultraviolet region (~270 nm) originating from the exciton-shifted van Hove Singularities in graphene density of states (DOSs) [4]. Another key parameter that defines the role of graphene in optoelectronics is optical conductivity. Since the light absorption in graphene occurs in both inter- and intraband transitions, as shown in Figure 1.2a, optical conductivity is the combination of inter- and intraband conductivities [4].

Ultrafast optical pulses generate a nonequilibrium carrier population in both valence and conduction bands. The cooling or bringing these excited carriers to equilibrium with lattice consists of two cooling steps, ultrafast carrier–carrier intraband collisions followed by phonon emissions and a slower cooling that corresponds to electron interband relaxation and cooling of hot phonons [6]. At low frequencies or low photon energies, the intraband transitions dominate, and interband transitions dominate in graphene at high frequencies. Further increasing the frequency, the optical conductivity reduces to a constant value $e^2/(4\hbar)$ that includes the visible region, resulting in the universal absorbance of ~2.3% for graphene as displayed in Figure 1.2b. The dependence of optical conductivity on carrier concentration or the Fermi level allows electrostatically controlling optical absorption. For instance, in the infrared region, the optical absorption can be slightly varied from 0% to 2.3%, leading to tunable devices such as IR modulators, phase shifters, beam steerers, and mode-lock lasers [5].

## 1.3 Emergence of Graphene in Silicon Optoelectronics

Optoelectronics based on 2D materials integrated with the CMOS process is the most growing area of 2D electronics in the present decade (Figure 1.1), where

graphene-based devices dominate both in terms of investigating fundamental physics and developing real-world applications. 2D material-integrated optoelectronics such as cameras and spectrometers are already on the verge of commercialization [2]. Next in the row are optical modulators and photodetectors that are gaining the attention of many researchers. Here, we discuss these emerging applications and concepts of graphene-based optoelectronics compatible with CMOS integration in back-end-of-line (BEOL) and front-end-of-line (FEOL). The complexity of integration increases from BEOL to FEOL. Therefore, most of the existing device schemes of 2D material-based optoelectronics are compatible with the BEOL process [2]. We start our discussion with the role of graphene in BEOL optoelectronics.

The simple transfer process, transparent yet high carrier mobility, and mechanically robust while flexible are graphene's critical merits that allow easy integration with Si CMOS technology in the BEOL fabrication stage. In 2D optoelectronics, most image sensors, spectrometers, modulators, and photodetectors are based on BEOL and show higher potential for commercialization, as shown in Figure 1.1. The cost of image sensors and spectrometers in infrared and terahertz regions is very high. The integration of conventional infrared sensors in Si CMOS is complex and not monolithic. Graphene offers immediate benefits in this sector, leading to low-cost ultrafast optical modulation, extreme broadband photodetection (ultraviolet – terahertz), high-performance LEDs, and data communications [2, 4, 5]. Some of these applications and their working principles are discussed here.

## 1.4 Photodetection in Graphene

Graphene photodetectors are first categorized based on the intrinsic mechanism combined with the role of graphene and silicon. The intrinsic device mechanism plays a crucial role in developing the device scheme for integrating graphene with the CMOS circuit. Here, we discuss some well-studied graphene photodetection mechanisms and related 2D material-based photodetectors such as photovoltaic, bolometric, photothermoelectric (PTE), photogating, and plasmon-wave-assisted mechanisms [5, 7]. The photovoltaic effect emerges from the built-in electric field at graphene–metal interfaces, gate-induced potential differences, or spatially nonuniform intrinsic doping in graphene, whereas, if the incident light induces local variation in temperature resulting in a change in resistance followed by the current passing through the device in the presence of an electric field, it is termed as bolometric effect. On the other hand, the PTE effect refers to a light-induced thermal gradient across the junction of two materials with different Seebeck coefficients.

In a phototransistor structure, when graphene is used as a channel, a finite DC voltage can be generated in the device as a response to the oscillating radiation field in a plasma wave-assisted photodetection mechanism. Here, graphene acts as a cavity for plasma waves – collective density oscillations. To be specific, when the plasma waves are weakly damped, in other words when the plasma waves launched in one of the electrodes of the graphene channel propagate to the other electrode within

the momentum relaxation time, then these plasma waves form standing waves, leading to resonantly enhanced response [5, 7]. The physical mechanism and crucial parameters of these different types of photodetection in graphene are discussed in detail below, which are the key mechanisms to understand the role of graphene in Si CMOS-integrated photodetection.

### 1.4.1 Performance Metrics

To evaluate the performance of photodetectors and compare them with other detectors, it is essential to understand some of the crucial performance metrics such as responsivity $(\mathcal{R})$, quantum efficiency ($\eta$), response time, and noise equivalent power (NEP). We briefly discuss these parameters to understand the general concepts associated with the photodetector. First, we consider the power of the incident light on the photodetector as $P$ with the photon energy, $E_{\text{Ph}} = h\vartheta$. Then, we can estimate the photon flux, $\Phi = P/h\vartheta$. Based on the operating mode, the photovoltage or photocurrent can be defined as $\Delta V = V_l - V_d$ or $I_{\text{pc}} = I_l - I_d$. In the same way, the responsivity can be defined in terms of either photocurrent or photovoltage,

$$\mathcal{R} = I_{\text{pc}}/P \text{ or } \mathrm{DV}/\mathrm{P} \tag{1.2}$$

The external quantum efficiency is the ratio of photoinduced charges per second to the number of incident photons per second,

$$\eta_{\text{ext}} = \left(\mathrm{PC}/e_o\right)/\Phi \tag{1.3}$$

In the same way, the internal quantum efficiency (IQE) is defined by considering the number of photons absorbed instead of the total incident photons,

$$\eta_{\text{int}} = \left(\mathrm{PC}/e_o\right)/\Phi_{\text{abs}} \tag{1.4}$$

Here, $\Phi_{\text{abs}}$ is the total absorbed photon flux. IQE can also be used to calculate the current gain of a photodetector.

The characteristic time of a photodetector to switch between the illuminated (ON) and dark state (OFF) is known as photoresponse or photoswitching time. The bandwidth $B$ of the photodetector can be defined as the cutoff frequency of the photodetector $f_c \approx 0.55/\tau$ but often limited by the RC time constant of the circuit [8]. NEP corresponds to the incident optical power required to produce the signal-to-noise (SNR) ratio of one in 1 Hz bandwidth.

### 1.4.2 Photovoltaic Effect

The photovoltaic effect generally emerges when photogenerated carriers are separated and transported due to the built-in potential in the photoactive material. This built-in or internal electric field can be created either by contacting a semiconductor

with metal as a Schottky junction or between differently doped (n- or p-type) semiconductors as a p–n junction [7]. These devices, in principle, function in both photovoltaic and photoconductive modes. The external bias is zero in PV mode, and the only electric field is internal. Thus, the current measured in this mode is the short-circuit current ($I_{sc}$). In the open-circuit mode, the generated photocarriers accumulate at the terminals to compensate the built-in electric field, leading to finite open-circuit voltage ($V_{oc}$), often used to measure the generated electrical power in solar cells. The lower dark current in this mode allows higher specific detectivity and lower NEP [2, 4, 7].

Photoconductive mode is activated in the device when a finite bias is applied to the terminals, which is commonly observed in Schottky diodes and p–n junctions in reverse bias. In this mode, photocarriers are quickly swept out of the device, leading to higher photocurrent, and hence exhibit lower response time and higher responsivity than in photovoltaic mode. The combination of photoconductive and PV affect has been observed in both planar and vertical junctions of metal–graphene and other graphene–2D planar junctions. In the case of PV effect in electrostatically doped p–n junctions of graphene or related 2D material, the typical width of the in-plane depletion region extends in the range of 200 nm, facing challenges with relatively low efficiencies (>30%) as difficult to maintain large depletion widths to capture the photogenerated carriers, where a large fraction of carriers recombine before moving into either the p or the n region [9, 10]. Vertical junctions formed by graphene and related 2D heterostructures circumvent these issues like the depletion region confines within one or two atomic thicknesses of 2D materials and extends for the entire area of the 2D junction. For instance, Schottky junctions made of graphene-TMDs can accommodate large built-in fields, reaching responsivity larger than $10\,\mathrm{mA\,W^{-1}}$ and IQEs of ~30% [11]. Much larger responsivities and IQEs have been observed in vertical 2D heterostructures, mostly due to their large active area.

### 1.4.3 Photoemission in Graphene Schottky Junctions

The most basic physical concept that needs to be understood in this context is the electron emission mechanism in heterointerfaces of graphene and other related 2D materials, their multilayers, and heterostructures, along with bulk 3D systems. The initial understanding of 2D-based interfaces and junctions relies on classic thermionic and field-emission theories, such as Richardson–Dushman and Fowler–Nordheim models [11]. However, electron emission in 2D materials and their interfaces is significantly different from bulk materials that have to be incorporated in transport models. Several models describing the charge transfer at 2D interfaces propose fundamentally different charge-transfer mechanisms. Therefore, it is essential to understand the difference between these models and the classic thermionic and field-emission models. A brief discussion is provided in this chapter on various charge transport models of 2D interfaces, with an emphasis on graphene-based Schottky junctions.

Another challenge in this area is identifying the dominating emission mechanism that decides the different charge transport and emission mechanisms at the

interface. In any Schottky junction, there are three main electron emission pathways, (i) thermionic emission, (ii) quantum mechanical tunneling, and (iii) photoemission. We first discuss these three emission pathways in graphene-Schottky junctions in different conditions and explain the differences between these models and the classical electron emission models. In general, multiple electron emission mechanisms can coexist simultaneously, thus identifying that the dominating emission mechanism is crucial for designing a device with optimum performance. The coupling of multiple emission mechanisms reveals exciting charge transport phenomena such as the photoenhanced thermionic emission – a combination of thermionic emission and photoemission, leading to the detection of photons with energies lower than the potential barrier at Schottky interfaces.

In the same way, when the photoemission is coupled with field emission, a photoassisted field emission emerges, or a thermal-assisted field emission dominates at a finite temperature. Electron emission dynamics are also dependent on the parameters of the incident laser and applied bias across the interface, where ultrafast laser with optimum pulse width and intensity can enhance the coupling between different emission mechanisms in materials such as graphene with unique electronic properties. In such conditions, novel quantum mechanical phenomena such as photothermionic (PTI) emission, multi-photon field emission, and dynamical optical field emission can be investigated in solid state systems. In the case of large interface currents, the electron emission is limited by the space charge, where the electric field of the charge carriers in transit restrains further charge transfer at the interface.

### 1.4.4 Thermionic Emission in Graphene-based Interfaces

Heating electrons in a material to overcome the potential barrier is defined as thermionic emission, a fundamental physical process in electronic devices. This leads to various functionalities in electronics, optoelectronics, and energy conversion. In thermionic emission, electrons are thermally excited to overcome the potential barrier in a heterostructure. The probability of occupation in higher energy states for an excited electron can be estimated by the Fermi–Dirac distribution. There are different ways to excite electrons in a system, such as thermal excitation, photoexcitation, and scattering of electrons in the presence of the electric field. In all these processes, when the excited electrons are in thermal equilibrium with the lattice, the emission process can be described with the thermionic emission model. By analyzing the charge density ($J$) as a function of applied bias, the charge transport in a Schottky junction can be approximated by the simple diode equation,

$$J = J_0\left(e^{\left(qV/\eta kT\right)} - 1\right),\ J_0 = A^* T^2 e^{-\Phi_B/kT} \tag{1.5}$$

where $J_0$ is the reverse saturation current density, $q$ is the elementary charge, $\eta$ is the ideality factor, $k$ is the Boltzmann constant, $V$ is the applied bias, $T$ is the temperature, $\Phi_B$ is the Schottky barrier height, and $A^*$ is the effective Richardson's constant. The ideality factor $\eta$ is used to determine the quality of the Schottky interface, and

**Table 1.1** Comparison of properties of 2D and bulk materials.

| Property | Bulk material | 2D material |
|---|---|---|
| Crystal periodicity | Well defined in all 3D | Well defined only in 2D |
| *E*–*k* dispersion | Parabolic | Parabolic/linear |
| Electrical contact | No qualitative difference | Different (edge/surface) |
| Electron *k*// component | Strictly conserved | Nonconserved |

high-quality graphene interfaces often show near-unity ideality factor. In a metal–semiconductor Schottky junction, the barrier height is constant for reverse bias current, indicating Fermi-level pinning due to large interface states, whereas in graphene–Schottky junction, for low-energy electrons, the Dirac cone approximation provides a reliable model for thermionic emission in graphene. It is essential to evaluate the limitations of the thermionic model for 2D materials. The validity of the Richardson–Dushman thermionic emission model in 2D materials must be carefully scrutinized. Table 1.1 presents the critical differences between bulk and 2D materials. The schematic drawings of one-dimensional edge contact and 2D surface contact of graphene are shown in Figure 1.3a. The initial models inspiring these studies are from semiconductor quantum well structures as displayed in Figure 1.3b.

The general assumptions of the RD thermionic emission model are listed below.

1) Electrons follow parabolic energy–momentum dispersion.
2) Crystal periodicity is uniform in all directions. Thus, electrically contacting 3D material in any order does not change the thermionic emission mechanism.
3) The tunneling probability of electrons can be expressed entirely as a function of the out-of-plane component of the momentum ($k_z$).

For graphene, due to finite DOSs at the Dirac point, much lower $A^*$ (in the order of $10^{-2}$ A cm$^{-2}$ K$^{-2}$) than the theoretical value of 112 A cm$^{-2}$ K$^{-2}$ have been observed and thus can be represented by the Landauer transport model as represented by the equation,

$$J = \frac{q}{\tau}\int_{\infty}^{-\infty} T(E)D(E)\left(f_{\mathrm{g}} - f_{\mathrm{Si}}\right)dE \tag{1.6}$$

where $\tau$ is the carrier injection time at the contact, $T(E)$ is the transmission probability over the Schottky barrier $\Phi_B$, $D(E)$ is the DOSs of graphene, and $f_{\mathrm{g}}$ and $f_{\mathrm{Si}}$ are the Fermi–Dirac functions of graphene and silicon, respectively. By incorporating the Landauer transport model in $J_0$ as shown below, the standard diode Eq. (1.5) can be applied to the graphene–Schottky junctions,

$$J_0 = \left[\frac{qD_o}{\tau}\left(kT\right)^2\left(\frac{\Phi_B}{kT}+1\right)\right]e^{-\Phi_B/kT} \tag{1.7}$$

The additional temperature dependence in Eq. (1.7) is the main difference with $J_0$ in Eq. (1.5). The experimental studies show that the Richardson–Schottky model

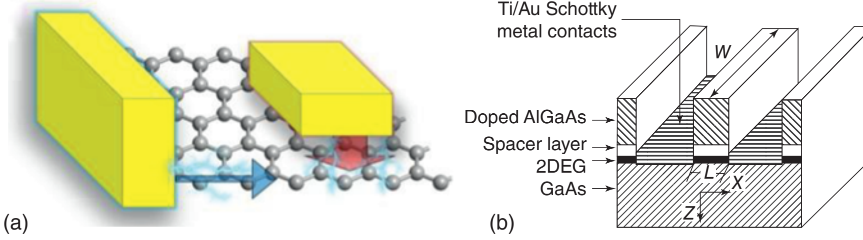


**Figure 1.3** (a) Schematic drawing of the one-dimensional edge and two-dimensional surface contact to graphene. (b) Schematic of the initial model of side-way thermionic charge injection of quasi-2D-electron gas in a semiconductor quantum well structure. DEG, dimensional electron gas. Source: Ang et al. [11]; John Wiley & Sons/CC BY SA 4.0.

and the Landauer transport model are indistinguishable as the dominant temperature dependence comes from the $e^{-\Phi_B/kT}$ in both the models. However, since this model mainly considers the limited DOS of graphene near the Dirac point, it is only suitable for low-energy range when $\Phi_B >> kT$ and the low energy of excited carriers. A significant deviation in the fitting of the experimental data with this model has been observed for higher energy excited carriers much above the Dirac point [11].

### 1.4.5 Hot Electron-based Photodetection

In photocarrier-driven detectors, optical transitions between excited and ground states are crucial as well as with a finite energy gap, whereas in the case of thermally driven detectors, both inter- and intraband transitions can contribute to the resulting photocurrent, eliminating the need for photon energy threshold and therefore exhibiting a large spectral responsivity. One of the pathways for relaxation of these exciting carriers is via carrier–carrier scattering resulting in the redistribution of energy within the electronic system leading to electronic bath temperature. Such a rise in average carrier temperature can generate a photocurrent or -voltage, leading to various hot-electron-based photodetection mechanisms such as PTE effect, bolometric effect, and PTI emission. The redistribution of excited carrier energy between the surrounding carriers can be viewed as thermalization within the electronic system but does not necessarily include lattice heating and thus can be represented by Fermi–Dirac distribution with elevated average electronic temperature. The overall ultrafast photocarrier dynamics are depicted in Figure 1.4. Photoexcitation in graphene can happen within <50 fs of ultrashort light pulse, followed by carrier–carrier scattering that induces carrier multiplications and raises the electron temperature higher than ambient temperature ($T_e > T_0$). The total carrier relaxation or cooling includes emission of strongly coupled optical phonons at hot-electron energies higher than ~200 meV, followed by acoustic phonons at low- energy range. How different stages of hot electron cooling leads to various photoresponse effects in graphene- based heterostructures are discussed below.

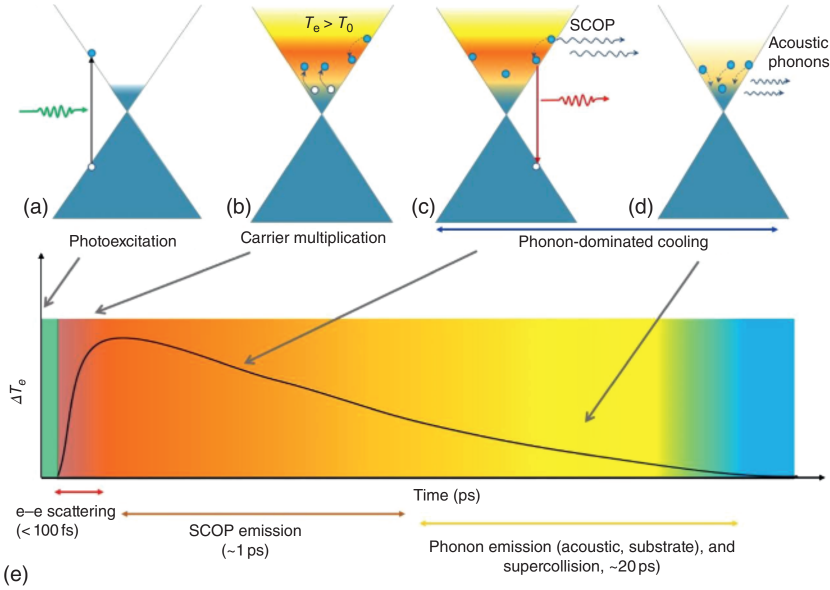


**Figure 1.4** Ultrafast photocarrier dynamics in graphene. (a) Photoexcitation in graphene with the incident of ultrashort light pulse (<50 fs). (b) Carrier–carrier scattering induces carrier multiplications and raises the electron temperature higher than the ambient temperature ($T_e > T_0$). Carrier relaxation or cooling in ~1.3 ps via emission of (c) strongly coupled optical phonons (SCOP) at hot-electron energies higher than ~200 meV and (d) acoustic phonons at low-energy range. (e) Evolution of differential electron temperature in the time domain.

#### 1.4.5.1 Photothermoelectric Effect (PTE)

If the light absorbed in a part of the photoactive material heats the electronic temperature $T_e$, a thermal gradient $\nabla T_e$ emerges between the hot and cold ends of the material, resulting in a finite potential gradient $\nabla V$ originating from the net charge imbalance from the thermal diffusion of carriers. The relation between $\nabla V$ and $\nabla T_e$ is proportional to the Seebeck coefficient as

$$\nabla V = S\ \nabla T_e \tag{1.8}$$

For metals, the Mott formula can be used to estimate the Seebeck coefficient:

$$S = -\frac{\pi^2 k_B^2 T_e}{3e_0} \frac{1}{\sigma\left(E_F\right)} \frac{\partial\sigma\left(E\right)}{\partial E}\Bigg| \tag{1.9}$$

Here, $\sigma(E)$ is the energy-dependent conductivity. The above formula is valid only for $k_B T_e << E_F$.

The PTE effect is an effective mechanism for realizing zero-bias photoresponse in various 2D materials, including graphene [12–14]. The first demonstration of the PTE effect in 2D materials is made in a device with the interface of single- and bilayer graphene, where under light illumination, the difference in Seebeck coefficients of these two regions generates the potential gradient for the PTE effect.